Available online at www.sciencedirect.com
SCIENCE DIRECT®
Journal of Computational Physics 216 (2006) 430–453
JOURNAL OF COMPUTATIONAL PHYSICS
www.elsevier.com/locate/jcp

A fast algorithm for modeling multiple bubbles dynamics

T.T. Bui [a], E.T. Ong [b], B.C. Khoo [a,c,*], E. Klaseboer [b], K.C. Hung [b]

[a] *Department of Mechanical Engineering, National University of Singapore, 9 Engineering Drive 1, Singapore 117576, Singapore*
[b] *Institute of High Performance Computing, 1 Science Park Road, #01-01 The Capricorn, Singapore Science Park II, Singapore 117528, Singapore*
[c] *High Performance Computation for Engineered Systems, Singapore – MIT Alliance, 4 Engineering Drive 3, Singapore 117576, Singapore*

Received 15 June 2005; received in revised form 8 December 2005; accepted 16 December 2005
Available online 25 January 2006

Abstract

This work presents the development of a numerical strategy that combines the fast Fourier transform on multipoles (FFTM) method and the boundary element method (BEM) to study the physics of multiple bubbles dynamics in moving boundary problems. The recent FFTM method can be employed to speedup the resolution of the boundary integral equation. However, one major drawback of the method is that its efficiency deteriorates quite significantly when the problem is spatially sparsely populated, as in the case where multiple bubbles are well separated. To overcome this deficiency, a new version of FFTM with clustering is proposed (henceforth called FFTM Clustering). The new algorithm first identifies and groups closely positioned bubbles. The original FFTM is then used to compute the potential contributions from the bubbles within its own group, while contributions from the other separated groups are evaluated via the multipole to local expansions translations operations directly. We tested the FFTM Clustering on several multiple bubble examples to demonstrate its effectiveness over the original FFTM method and vast improvement over the standard BEM. The high efficiency of the FFTM Clustering method allows us to simulate much larger multiple bubbles dynamics problems within reasonable time. Some physical behaviors of the multiple bubbles are also presented in this work.

Keywords: Bubble dynamics; Boundary integral method; Multipole approximations; Fast Fourier transform on multipoles

1. Introduction

A better understanding of the physics of multiple bubble dynamics is important for a wide range of applications including underwater explosions, biomedical and chemical processes [1–7]. Numerical modeling and simulation has proven to be an effective approach to study the complex phenomena of multiple bubbles dynamics. Boundary element method (BEM) is one effective numerical tool for solving such dynamical boundary value problem, with previous works by Blake and Gibson [1], Guerri et al. [7], Wang et al. [8,9], Zhang et al. [10], Wang [11], Rungsiyaphornrat et al. [12], Best and Kucera [13] and others.

* Corresponding author. Tel.: +65 68742889; fax: +65 67791459.
E-mail address: mpekbc@nus.edu.sg (B.C. Khoo).

0021-9991/$ - see front matter
doi:10.1016/j.jcp.2005.12.009

BEM has the distinct feature of reducing the problem dimension by 1, that is, only the boundaries of the bubbles and structures need to be discretized, and this greatly simplifies the pre- and post-processing tasks. Unfortunately, conventional BEM generates a dense matrix system, which requires $O(N^2)$ memory storage requirements and operations to solve with iterative methods [14,15]. This poses new challenges, and also provides the motivation to devise more efficient methods, to the simulations of large-scale problems, such as in multiple bubble dynamics, where N can easily exceeds several thousands.

Numerous fast algorithms were developed over the last few decades, including the hierarchical-based tree algorithm [16,17], fast multipole method (FMM) [18–20], and the FFT-based methods such as the particle–particle–particle-mesh (PPPM) methods [21], precorrected-FFT approach [22] and the recent fast Fourier transform on multipoles (FFTM) [23,24]. The efficiency of the former group comes from the use of multipole expansions theories and a highly effective hierarchical structure, where multipole and local expansions are translated efficiently up/down the oct-tree when evaluating the far field potentials. As for the FFT-based methods, the speedup is gained from the use of FFT algorithms [25] for computing the discrete convolutions. Other fast techniques include the sparsification of the dense matrix systems by using singular value decomposition (SVD) [26], wavelet transforms [27] and the multilevel methods for the fast solution of integral equations [28].

In this paper, the fast Fourier transform on multipoles (FFTM) coupled with BEM is implemented to solve the boundary integral equation that governs the dynamics of multiple bubbles. However, its efficiency suffers significantly when the problem is spatially sparse, that is, quite a substantial portion of the problem domain is empty (for example, in the case where the bubbles were placed widely apart). Here, we suggest an improvement with a clustering approach. The new algorithm first identifies and groups closely positioned bubbles, based on their relative distances. Then the elements interactions within the groups itself are evaluated rapidly using FFTM, while interactions among the different groups are evaluated directly via multipole to local translation operations. It is demonstrated that the new approach can performs significantly faster than the original FFTM method without compromising the accuracy.

This paper is organized as follows. Sections 2 and 3 briefly outline the mathematical formulation of the bubble dynamics simulation model, and the mathematical preliminaries of the multipole approximations theories, respectively. In Section 4, the FFTM and the FFTM Clustering algorithms are presented for the bubble dynamics problem. Then in Section 5, we present some numerical studies on the accuracy and effectiveness of the FFTM Clustering method. In Section 6, we study the physics of multiple explosion bubbles. Finally, the major findings of this study are summarized in Section 7.

2. Mathematical formulation of the bubble dynamics model

2.1. Boundary integral equation for potential flow problem

Assume that the fluid domain around the bubbles is inviscid, incompressible and irrotational, the governing equation for such a flow is the Laplace equation, i.e. $\nabla^2\Phi = 0$, where Φ is the velocity potential and the velocity vector is defined as $\boldsymbol{u} = \nabla\Phi$. Using Green's theorem, the problem can be rewritten as the following boundary integral equation:

$$c(\boldsymbol{x})\Phi(\boldsymbol{x}) = \int_\Gamma \left[\frac{\partial\Phi(\boldsymbol{y})}{\partial n}\frac{1}{\|\boldsymbol{x}-\boldsymbol{y}\|} - \Phi(\boldsymbol{y})\frac{(\boldsymbol{x}-\boldsymbol{y})\cdot\boldsymbol{n}}{\|\boldsymbol{x}-\boldsymbol{y}\|^3}\right]\mathrm{d}\Gamma(\boldsymbol{y}), \tag{1}$$

where $\boldsymbol{x}$ and $\boldsymbol{y}$ correspond to the field and source points, respectively, $\boldsymbol{n}$ is the normal vector directed away from the fluid, and $c(\boldsymbol{x})$ is the solid angle defined at the location $\boldsymbol{x}$. Applying the collocation BEM scheme to Eq. (1), with the geometry and the physical variables being approximated by discrete linear triangular elements, leads to a discrete model defined by its nodal variables. Finally, applying the appropriate boundary conditions leads to a dense linear system of equations. As mentioned above, solving the dense matrix system becomes computational intensive for large-scale problems. In Section 4, we present the FFTM algorithms that can solve the problem more efficiently, with minimal loss in accuracy.

2.2. Bubble model in dimensionless form

Assume that the bubbles contain non-condensable ideal gas, and the expansion and compression of the gas are adiabatic. Then, the gas pressure P inside each bubble can be expressed in term of the current volume V as

$$P = P_0\left(\frac{V_0}{V}\right)^{\lambda}, \tag{2}$$

where P_0 and V_0 are the bubble initiate pressure and volume, respectively. The parameter λ is the ratio of specific heats which is 1.25 (used in this study throughout) for the gaseous explosion products resulting from a TNT explosion [5]. For non-dimensionalization purpose, the maximum radius R_m of one of the bubbles [12] in the system is chosen to be the scaling factor for all lengths. The reference pressure P_{ref} at a depth H, given by $P_{ref} = P_\infty + \rho g H$, where g is the gravitational acceleration, P_∞ is the atmospheric pressure, and ρ is the density of the surrounding fluid, is the scaling factor for all pressures. The other scaling factors for the velocity potential, velocity and time are: $\Phi_{ref} = R_m\sqrt{P_{ref}/\rho}$, $u_{ref} = \sqrt{P_{ref}/\rho}$ and $t_{ref} = R_m\sqrt{\rho/P_{ref}}$, respectively. The bubble pressure in dimensionless form becomes

$$P' = \varepsilon\left(\frac{V'_0}{V'}\right)^{\lambda}, \tag{3}$$

where the dimensionless strength parameter ε is defined as $\varepsilon = P_0/P_{ref}$. In this study, the strength parameter for all the bubbles presented is $\varepsilon = 97.52$. The initial radius of the first bubble is chosen to be $R'_0 = 0.1499$, those of the subsequent bubbles can be different from this value. Ignoring gravitational and surface tension effects, the bubble deforms with time according to the following dynamic and kinematics conditions [12]:

$$\frac{D\Phi'}{Dt'} = 1 - P' + \frac{1}{2}|\boldsymbol{u}'|^2, \tag{4}$$

$$\frac{D\boldsymbol{x}'}{Dt'} = \boldsymbol{u}'. \tag{5}$$

Eq. (4) is the dimensionless unsteady Bernoulli equation at the bubble interface and it is used to update the velocity potential Φ' as the bubble evolves. The nodal positions of the bubble surfaces $\boldsymbol{x}'$ are updated with the kinematic condition in Eq. (5).

To maintain the stability of the numerical solution, the time-step size is controlled such that the changes in potential are bounded at each time step. For most simulations, at each subsequent time step $\Delta t'$ the following criterion is used [9]:

$$\Delta t' = \frac{\delta}{\max\left|1 + \frac{1}{2}|\boldsymbol{u}'|^2 + P'\right|}. \tag{6}$$

This procedure ensures that the maximum potential change anywhere is limited to a value of $\delta = 0.003$, which helps to avoid possible numerical instabilities. The initial condition assumes that the entire fluid is at rest, i.e. Φ' and $\partial\Phi'/\partial n$ are set to zero at $t' = 0$. This assumption is also applied to bubbles that are initiated at subsequent later times.

3. Multipole expansion approximation and boundary integral equation

Multipole expansion is an approximation technique for evaluating the far potential field due to distant sources. It is based on the multipole translation theory that was derived by Greengard and Rokhlin [18,19] in their implementation of the fast multipole method (FMM). In the following sections, we will briefly describe how the multipole approximation technique can be employed in our context. Readers can refer to [19,29] for details on the multipole translation theory.

3.1. Multipole and local expansions and their translation operators: a re-visit

Given a set of n_e boundary elements, which are clustered about point $\boldsymbol{O}$ and bounded within a sphere S_a of radius a. Single layer and dipole layer sources (corresponding to the first and second terms in the integral in

Eq. (1), respectively) are distributed on the surface of each element. Consider a potential evaluation point $\boldsymbol{x}$ (corresponding to a node on the bubbles) that is near a point $\boldsymbol{O}^*$ and bounded within a sphere S_b of radius b. Note that these spheres are just fictitious bounds, and are not related directly to the geometries of the bubbles. Now, the exact potential at the evaluation points $\boldsymbol{x}$ due to the set of elements n_e are given by

$$\Phi_{\text{exact}}(\boldsymbol{x}) = \sum_{j=1}^{n_e} \int_{\widehat{\Gamma}_j} \frac{\partial \Phi(\boldsymbol{y})}{\partial n} \frac{1}{\|\boldsymbol{x}-\boldsymbol{y}\|} \mathrm{d}\Gamma(\boldsymbol{y}) \quad \text{for a single layer source} \tag{7}$$

and

$$\Phi_{\text{exact}}(\boldsymbol{x}) = \sum_{j=1}^{n_e} \int_{\widehat{\Gamma}_j} \Phi(\boldsymbol{y}) \frac{(\boldsymbol{x}-\boldsymbol{y})\cdot\boldsymbol{n}}{\|\boldsymbol{x}-\boldsymbol{y}\|^3} \mathrm{d}\Gamma(\boldsymbol{y}) \quad \text{for a double layer source,} \tag{8}$$

where $\widehat{\Gamma}_j$ represents the discrete boundary elements. Next, we will describe how multipole expansion is used to approximate the integrals in Eqs. (7) and (8).

Now, suppose the relative distance between $\boldsymbol{O}$ and $\boldsymbol{O}^*$ is significantly larger than $(a+b)$, then the potentials in Eq. (7) and (8) can be approximated by the local expansion,

$$\Phi_{\text{multipole}}(\boldsymbol{x}) = \sum_{j=0}^{P_{\text{exp}}} \sum_{k=-j}^{j} L_j^k Y_j^{-k}(\theta^*, \varphi^*) r^{*j}, \tag{9}$$

where P_{exp} is the order at which the expansion is truncated, $(r^*, \theta^*, \varphi^*)$ is the relative position of $\boldsymbol{x}$ with respect to $\boldsymbol{O}^*$. Here, $Y_n^m(\theta,\varphi) = \sqrt{\frac{(n-|m|)!}{(n+|m|)!}} P_n^{|m|}(\cos\theta)\mathrm{e}^{\mathrm{i}m\varphi}$ is the spherical harmonics function of degree n and order m, with $P_n^{|m|}(\cos\theta)$ being the associated Legendre function of the first kind [30].

The local expansion coefficients L_j^k, i.e. the potential gradients at $\boldsymbol{O}^*$ due to the multipole moments M_n^m sources defined at $\boldsymbol{O}$, are derived using

$$L_j^k = \sum_{n=0}^{P_{\text{exp}}} \sum_{m=-n}^{n} \mathrm{i}^{|k-m|-|k|-|m|} \frac{A_n^m A_j^k Y_{j+n}^{m-k}(\alpha,\beta)}{(-1)^j A_{j+n}^{m-k} \rho^{j+n+1}} M_n^m, \tag{10}$$

where (ρ, α, β) represents the spherical coordinates of the vector $(\boldsymbol{O}^*\text{–}\boldsymbol{O})$, $\mathrm{i} = \sqrt{-1}$ and $A_n^m = \frac{(-1)^n}{\sqrt{(n-m)!(n+m)!}}$. And the multipole moments M_n^m in Eq. (10) are defined by

$$M_n^m = \sum_{j=1}^{n_e} \int_{\widehat{\Gamma}_j} \frac{\partial \Phi}{\partial n}(\boldsymbol{y}) Y_n^{-m}(\theta,\varphi) r^n \mathrm{d}\Gamma(\boldsymbol{y}) \quad \text{for single layer source} \tag{11}$$

and

$$M_n^m = \sum_{j=1}^{n_e} \int_{\widehat{\Gamma}_j} \Phi(\boldsymbol{y}) \nabla(Y_n^{-m}(\theta,\varphi) r^n) \cdot \boldsymbol{n} \mathrm{d}\Gamma(\boldsymbol{y}) \quad \text{for double layer source,} \tag{12}$$

where (r, θ, φ) are the coordinates of $\boldsymbol{y}$ with respect to $\boldsymbol{O}$. Eqs. (11) and (12) are the operators that convert a set of continuous panels sources to discrete point sources defined at the centre of the sphere S_a.

Eqs. (9)–(12) are sufficient for the implementation of the FFTM algorithm. However, for the new FFTM Clustering method (see Section 4.3), we need two other important translation operators, namely the multipole-to-multipole and local-to-local translation operators. These operators translate the expansions coefficients, i.e. M_n^m and L_j^k from their original centre of expansion $\boldsymbol{O}$ to some arbitrary point $\tilde{\boldsymbol{O}}$. They are defined respectively by

$$\tilde{M}_j^k = \sum_{n=0}^{j} \sum_{m=-n}^{n} \frac{\mathrm{i}^{|k|-|m|-|k-m|} A_n^m A_{j-n}^{k-m} Y_n^{-m}(\tilde{\alpha},\tilde{\beta}) \tilde{\rho}^n}{A_j^k} M_{j-n}^{k-m} \tag{13}$$

and

$$\tilde{L}_j^k = \sum_{n=j}^{P_{\text{exp}}} \sum_{m=-n}^{n} \frac{\mathrm{i}^{|m|-|k|-|m-k|} A_{n-j}^{m-k} A_j^k Y_{n-j}^{m-k}(\tilde{\alpha},\tilde{\beta}) \tilde{\rho}^{n-j}}{(-1)^{n+j} A_n^m} L_n^m, \tag{14}$$

where $\tilde{M}_j^k$ and $\tilde{L}_j^k$ are the new sets of expansion coefficients defined at $\tilde{\boldsymbol{O}}$, and $(\tilde{\rho}, \tilde{\alpha}, \tilde{\beta})$ defines the shifting vector $(\tilde{\boldsymbol{O}}$–$\boldsymbol{O})$.

The translations of the multipole and local expansions are allowed provided the resulting bounding spheres for the sources and field points remain well separated. The error associated with the multipole expansion approximation is

$$|\Phi_{\text{exact}} - \Phi_{\text{multipole}}| \leqslant K\left(\frac{1}{\chi - 1}\right)\left(\frac{1}{\chi}\right)^{P_{\text{exp}}+1}, \tag{15}$$

where K is a constant related to the strengths of the sources field, and χ is a measure of the relative distance between the centers of the multipole expansion and local expansion.

3.2. Relationship between multipole expansion and boundary integral equation

In this section, we establish the relationship between the multipole expansion and the boundary integral Eq. (1). It may be mentioned that the link between the two methods is established only when iterative solution methods [14,15] are used. In this study, we chose GMRES iterative solver. In GMRES, one needs to compute the Krylov subspace vector $\boldsymbol{v}$ that spans the solution space at every iteration, and is of the form: $\boldsymbol{v} = [\boldsymbol{A}]\bar{\boldsymbol{u}}$, where $[\boldsymbol{A}]$ is a fully populated coefficient matrix that is derived from the boundary integral Eq. (1), and $\bar{\boldsymbol{u}}$ is related to the initial guess of the solution. This dense matrix–vector multiplication is obviously an $O(N^2)$ operation, which becomes computationally intractable when solving large-scale problems. Now, multipole expansion is an approximation technique that can be used to speedup this calculation step.

First, this step is equivalent to the potential field calculation of Eq. (1) for all the nodal locations $\boldsymbol{x}$. This suggests that the multipole expansions can be used to approximate the far field potential contributions from those elements sufficiently far from $\boldsymbol{x}$, as described above. For those elements that are near to $\boldsymbol{x}$, their effects are accounted for as in the conventional BEM approach. In other words, many "distant" elements potential contributions are approximated by the multipole expansions leading to vast savings in computations.

Two existing fast algorithms exploit this multipole approximation technique for boundary integral calculation of Eq. (1), namely the Fast Multipole Method (FMM) [19,20], and the recent Fast Fourier transform on Multipoles (FFTM) [23,24]. FMM devises a systematic hierarchical procedure employing the multipole and local expansions repeatedly, while FFTM expresses the computational intensive multipole to local translation operations as a series of discrete convolutions to be evaluated rapidly using FFT algorithms.

3.3. Providing good initial guesses for iterative solution methods

The bubble dynamics simulations require numerous time steps. Usually the time step size is fairly small, chosen according to Eq. (6) to avoid possible numerical instabilities. Since the time-step size is generally small, the changes in geometry of the bubbles and their surface velocities are expected to be small between successive time-steps. Therefore, the previous time steps solutions can serve to provide good initial guesses for future time step t_1 as follows:

$$\boldsymbol{v}(t_1)_{\text{guess}} = \frac{t_1 - t_0}{t_{-1} - t_0}\boldsymbol{v}(t_{-1}) - \frac{t_1 - t_{-1}}{t_{-1} - t_0}\boldsymbol{v}(t_0), \tag{16}$$

where t_{-1} and t_0 are the previous and current time-steps, respectively.

4. Fast Fourier transform on multipoles (FFTM) for bubble dynamics simulations

FFTM arises from an important observation that the multipole to local expansion translation operation in Eq. (10) can be expressed as a series of discrete convolutions of the multipole moments with their associated translation operators. The high efficiency of the algorithm is primarily due to employing the FFT algorithms, such as FFTW [31], to evaluate the numerous discrete convolutions. In the following section, we will briefly describe the FFTM algorithm in the context of the multiple bubbles dynamics simulations.

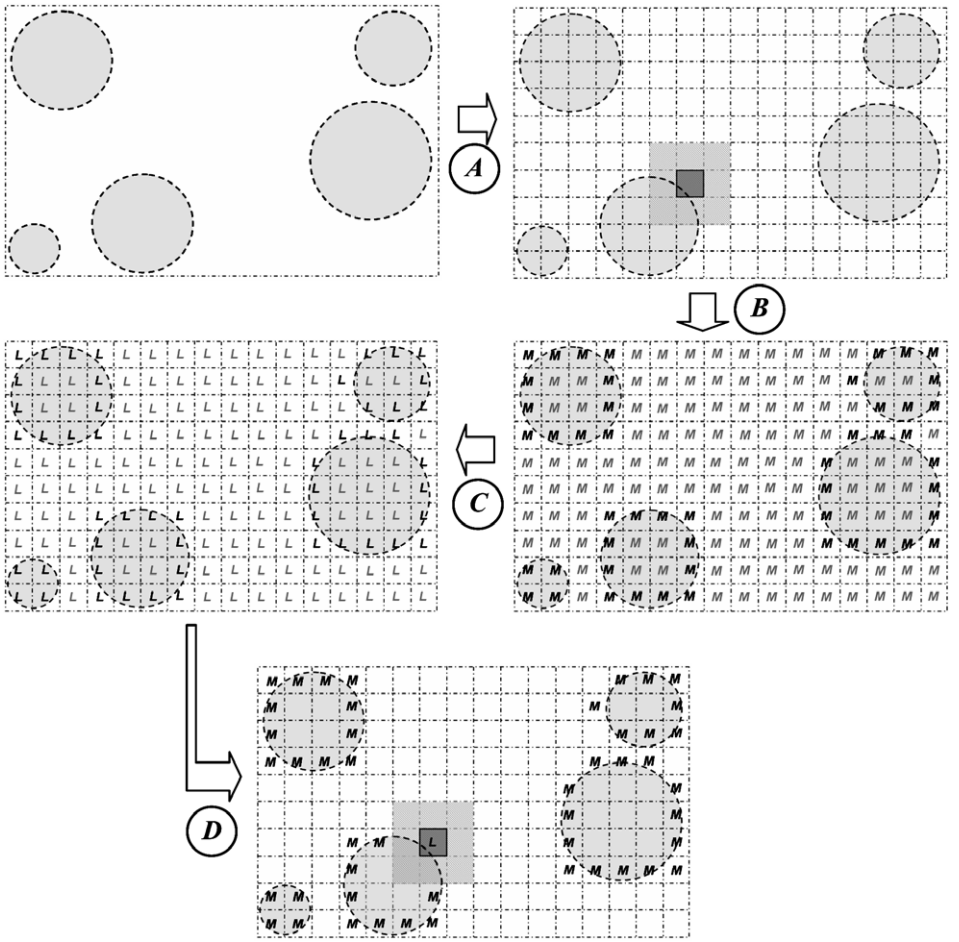

Fig. 1. Two dimensional illustration of the FFTM method. The letters A to D correspond to the four steps outlined in Section 4.1.

4.1. FFTM algorithm and its implementation

We shall illustrate the FFTM algorithm with a two-dimensional problem in Fig. 1, which comprises of five spherical bubbles of different sizes. The objective is to evaluate the potentials on the bubble surfaces due to the single layer and double layer sources as in Eq. (1). The FFTM algorithm comprises the following four steps, which are referred to as steps 'A' to 'D' (and thereafter) in Fig. 1.

A. *Spatial discretization*. This step subdivides the problem domain into many small cells, and then assigns the nodes and elements among these cells accordingly. It clearly differentiates the "near" and "distant" elements with respect to any given cell. The "near" elements potential contributions are calculated in the same manner as in standard BEM, while the "distant" ones are approximated by multipole expansions.

B. *Conversion of elements sources to multipole moments*. This step converts the clustered groups of elements within each of the cells into multipole moments $\boldsymbol{M}$. This is accomplished via the transformation operators given in Eq. (11) and (12).

C. *Calculating the local expansions due to multipole moments*. This evaluates the local expansion coefficients $\boldsymbol{L}$ at all the cells centers due to the multipole moments $\boldsymbol{M}$ via the multipole to local expansion translation operator in Eq. (10), and can be written as

$$L_j^k(y_1,y_2,y_3)=\sum_{n=0}^{P_{\exp}}\sum_{m=-n}^{n}\left[\sum_{x_1}\sum_{x_2}\sum_{x_3}M_n^m(x_1,x_2,x_3)*T_{j,n}^{k,m}(y_1-x_1,y_2-x_2,y_3-x_3)\right], \tag{17}$$

where $\boldsymbol{y} = (y_1, y_2, y_3)$ and $\boldsymbol{x} = (x_1, x_2, x_3)$ are the coordinates of the centroids of $\boldsymbol{L}$ and $\boldsymbol{M}$ cells, respectively, and $T_{j,n}^{k,m}(\boldsymbol{x}) = \mathrm{i}^{|k-m|-|k|-|m|} \frac{A_n^m A_j^k Y_{j+n}^{m-k}(\alpha,\beta)}{(-1)^j A_{j+n}^{m-k} \rho^{j+n+1}}$. Since these two sets of centroids coincide and are regularly positioned, the series of discrete convolutions can be evaluated rapidly using the FFT routines, such as FFTW [31].

D. *Calculating the potentials at nodal positions*. With the local expansion coefficients $\boldsymbol{L}$ computed at all the cells centers, the potentials at the nodal positions can be computed using the local expansion Eq. (9) for the "distant" elements contributions. The "near" elements effects are the added onto the nodal points directly. Next, we describe the implementation of FFTM for the bubble dynamics simulations which is divided into the initialization and iteration stages.

At initialization stage:

(i) Perform step *A* to allocate the nodes and elements among the cells.
(ii) Compute the various transformation matrices for all the non-empty cells. They are: (a) the boundary element to multipole moments transformation matrices (***B2M***) via Eqs. (11) and (12); (b) the local expansions coefficients to potential transformation matrices (***L2P***) via Eq. (9); and (c) the "near" elements coefficient matrices (***BEM***) using the boundary element integral equation.
(iii) Compute the Fourier transforms of the various translation operators $T_{j,n}^{k,m}$ in Eq. (17), which is denoted by $\boldsymbol{FFT}(T_{j,n}^{k,m})$.

The above-mentioned operators are dependent only on the geometry of the bubbles and hence are computed once and stored for repetitive used at the iteration stage of the GMRES iterative solver.

At iteration stage:

(i) Perform step *B* with ***B2M*** matrices, which transforms the boundary elements discretized problem to one containing multipole moments at regularly spaced grids.
(ii) Perform step *C* comprising the Fourier transforms of the multipole moments, followed by its element-wise multiplications with $\boldsymbol{FFT}(T_{j,n}^{k,m})$. This gives the $\boldsymbol{FFT}(L_j^k)$ whose inverse Fourier transforms gives the desired L_j^k.
(iii) Finally, perform step *D* using ***L2P*** with the information of L_j^k from (ii), and also adding the "near" elements contributions via ***BEM***.

4.2. Loss of efficiency in FFTM for spatially sparse problems

It was demonstrated for the electrostatics analysis [23,24] that FFTM is an efficient and accurate method. However, it suffers significant loss in efficiency when dealing with spatially sparse problems [24]. This deterioration in efficiency is largely due to the fact that FFTM has to perform calculations even for the empty cells.

On the other hand, FMM is noted to be hardly affected by this sparseness issue [19], since it ignores all the empty cells. This seems to suggest that FMM is a preferred fast solver for sparse problems over FFTM. However, due to the accuracy requirement, FMM requires significantly higher order of expansion than FFTM to achieve the same order of accuracy (see [24] for detailed discussions on this accuracy issue). An obvious impact is that the computational efforts for computing and storing the multipole and local expansion coefficients and also their related transformation matrices would be significantly much more expensive for FMM than FFTM, since they scale like $\mathrm{O}(P_{\mathrm{exp}}^2)$.

In this work utilizing FFTM, extensive numerical tests were carried out by Bui [32] to determine an optimum P_{exp}, the order in which the multipole approximation technique is truncated, to balance between accuracy and efficiency for the computation. It was found that $P_{\mathrm{exp}} = 4$ is a good choice which stills accords an accuracy of less than 1.0 % difference from the standard BEM. Hence, this is the expansion order used for the rest of the numerical examples in this study. One can refer to Bui thesis [32] for details of the tests.

4.3. FFTM Clustering method

From the above discussions, it seems that neither FMM nor FFTM is suitable for solving spatially sparse problems. To alleviate this sparseness issue, we propose the following FFTM Clustering method, which is essentially combining the FFTM and FMM algorithms. Here, we use the same example as used in Fig. 1 to explain the method. Basically, the method comprises the following steps (see Fig. 2).

(a) *Grouping of bubbles*. This step of the FFTM Clustering is to identify the closely packed bubbles and then group them separately. Two bubbles are considered "close" together if their relative distance between the centers d_{ij} is less than $D(r_i + r_j)$; where r_i and r_j are the radii of the spheres that bound the respective bubbles, and D is a constant factor that defines the breakeven point when the FFTM is as efficient as FFTM Clustering, for a given order of accuracy. An estimate of the D value is taken to be $D = 2(r_i + r_j)$. In this example, it is quite intuitive to group the bubbles as shown in Fig. 2(a), that is, G_1, G_2 and G_3.

(b) *Defining sub-groups for all groups*. The objective is to define sub-groups which form a hierarchical oct-tree. For this example, G_1 has only one sub-group, denoted by G_{11}, while G_2 and G_3 have two sub-groups each, denoted by G_{21} and G_{22} for G_2, and G_{31} and G_{32} for G_3, respectively. Note that the sub-groups formed for a given group are dependent on the spatial discretization (see step *A* of the FFTM algorithm) of that particular group. In general, it is defined by the ratio: (volume of the block that bounds the group)/(shortest dimension of the block). This is to facilitate the use of the various translation operators discussed in Section 3. Dummy cells are added to zero-pad the oct-trees, as denoted by **X** in Fig. 2(b). Note that oct-trees of the sub-groups may overlap each other (see sub-groups of G_2 and G_3), but each cell can only be associated with one sub-group.

(c) *Calculation of potential*. FFTM is firstly applied to each group to compute the potential contributions from the elements within its own respective groups. As for the potential contributions from the other groups, as an example, we consider only evaluating the local expansions of a particular cell in G_2 (as depicted in Fig. 2(c)) due to the multipole moments of G_1 and G_3. The procedures for computing the multipole interactions among the sub-groups are identical to that in FMM. These involve translating the multipole moments and local expansion coefficients up/down the hierarchical oct-trees, using Eqs. (13) and (14), respectively, and also the conversions of multipole to local expansions via Eq. (10). However, it is important to note that the number of multipole to local expansions conversion operations, which is the most computationally expensive part of the FMM algorithm, is not an issue here. This is because most of the multipole interactions would be at the coarser levels (since the sub-groups are well-separated), such as the situation shown in Fig. 2(c).

In the figure, the larger $\boldsymbol{M}$ correspond to the multipole moments at the lower levels of the oct-tree, which are used to compute the local expansion coefficients $\boldsymbol{L}$ at the respective levels. Finally, the local expansion coefficients $\boldsymbol{L}$ of the grey-colored cell are derived by summing the contributions from the FFTM computation of its self-group, and the local expansions from the higher level cell interactions due to multipole moments from the other groups.

It is observed that FFTM Clustering method incurred additional operations, but at the same time the costs of discrete convolutions calculations are also expected to be lesser than the original FFTM, particularly for the more spatially sparse problems. Hence, the clustering version would be more efficient only if the extra cost incurred does not exceed the saving it gets from computing the discrete convolutions. Below is a summary of the implementation of the FFTM Clustering method.

At initialization stage:

(i) Perform steps (a) and (b) to define the well-separated groups of bubbles, and also their respective sub-groups.

(ii) For each group, perform the steps associated with the initialization stage of the FFTM algorithm. On top of that, one needs to compute three more sets of transformation matrices, namely: multipole to multipole moments transformation matrices (***M2M***) via Eq. (13); multipole to local expansions transformation matrices (***M2L***) via Eq. (10); and local to local coefficients transformation matrices (***L2L***) via Eq. (14).

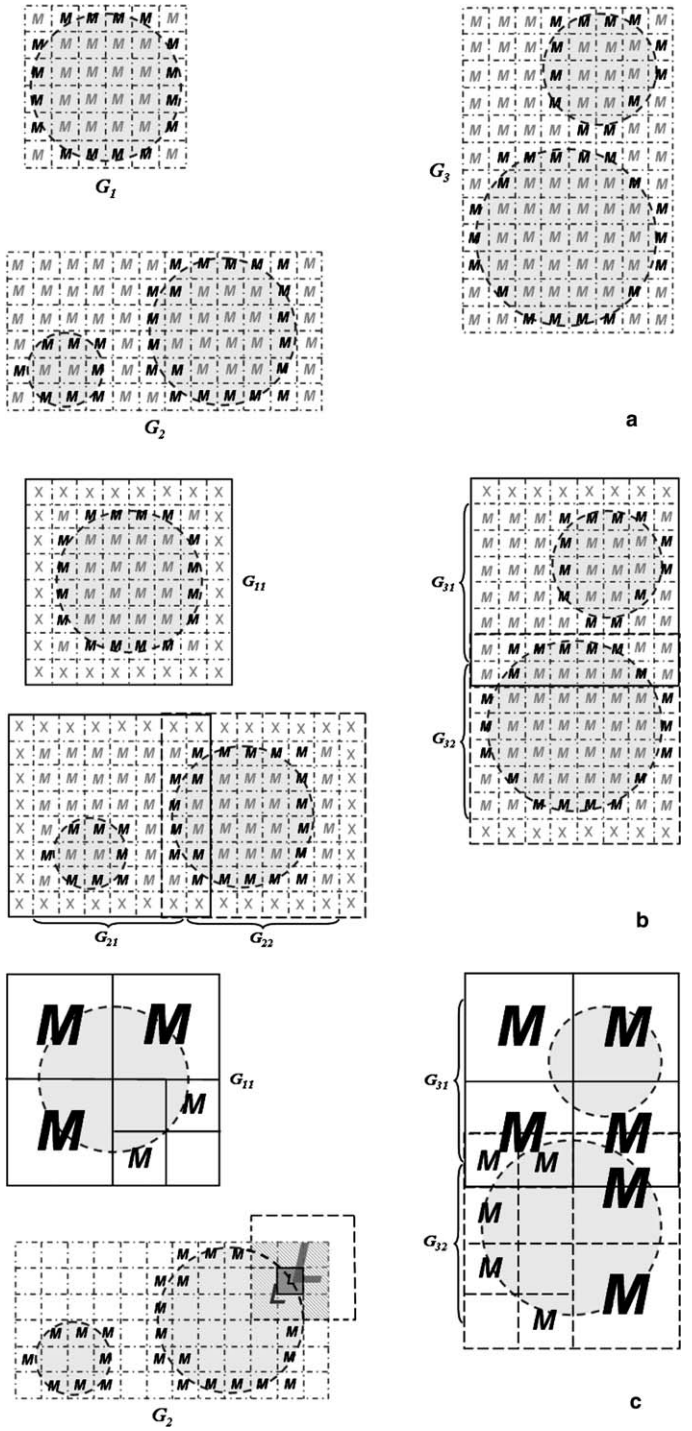

Fig. 2. Two dimensional illustration of the FFTM Clustering method. The letters (a), (b) and (c) correspond to the steps outlined in Section 4.3.

At iterative stage:

(i) For each group, perform the first two steps of the iteration stage in the FFTM algorithm. This gives the L_j^k at all the cells due to the elements within its self-group.

(ii) For each group, use ***M2M*** to translate the multipole moments M_n^m of each sub-groups down the hierarchical tree. Then use ***M2L*** to compute the sub-groups to sub-groups multipole interactions, to be followed via ***L2L*** to translate the local expansion coefficients upwards to the finest cells, which are added onto the L_j^k computed in the previous step (i).

(iii) Finally, perform the last step of the iteration stage in the FFTM algorithm to derive the potentials at all the nodal positions.

4.4. Critical distance

In this study, we aim to determine a critical distance at which the FFTM Clustering approach is more efficient than the original FFTM. This distance will then be taken to be the distance criterion for grouping the bubbles. The following examples were carried out on a single computer IBM p690 Regatta 1.3 GHz CPU speed, 2 Gbytes RAM with the convergence tolerance parameter equal to 10^{-5}.

Consider two spherical bubbles of radius $r_1 = r_2 = r = 1.0$, with the distance between their centers being D. The velocity potentials on each node on the two bubbles are set to be 1.0. Each bubble contains 642 nodes on the surface. The FFTM and FFTM Clustering methods are used to solve the problems with D varying from $2.5r$ to $6.0r$ for one time step. The average error incurred for the FFTM Clustering solver is measured with respect to the FFTM solver in the L_2 norm as

$$\text{Aver.Error} = \sqrt{\sum_{i=1}^{N}\left(\frac{\partial \Phi'}{\partial n}_{i,\text{FFTM\_Clustering}} - \frac{\partial \Phi'}{\partial n}_{i,\text{FFTM}}\right)^2 \Bigg/ \sum_{i=1}^{N}\left(\frac{\partial \Phi'}{\partial n}_{i,\text{FFTM}}\right)^2} \times 100\%, \tag{18}$$

where N is the total number of nodes.

Table 1 shows the comparison between the two methods in terms of their accuracy and CPU time taken. The CPU time taken by FFTM increases with D, whereas for FFTM Clustering, it reduces initially and then remains constant as the bubbles are placed further apart. It is observed that FFTM Clustering performs significantly better than FFTM with good accuracy when $D \geqslant 4r$. Hence, we suggest that the critical grouping distance between centers of two bubbles is $D = 2(r_1 + r_2)$, where r_1 and r_2 are the radii of the two bubbles.

5. Numerical results

In this section, we present some results on the FFTM and FFTM Clustering for bubbles simulation and compare with the standard BEM method in terms of accuracy and efficiency. By standard BEM, we refer to the direct BEM scheme with parametric triangular linear elements [11] where the dense matrix system is explicitly formed and then solved using an iterative method, such as GMRES. The time stepping scheme and the calculation of the normal vectors on the nodes were adopted from [11]. We have also included the geometrical least square smoothing and adaptive mesh refinement schemes by Zhang et al. [10] in our BEM solvers. For more details on the implementations of the standard BEM solver, readers are referred to the aforementioned works of Zhang et al. [10] and Wang [11]. In the following examples, all the bubbles were initially spherical at the insertion stage, and each bubble was discretized with 642 nodes and 1280 triangular linear elements. All the tests were carried out on a single computer IBM p690 Regatta 1.3 GHz as mentioned earlier.

Table 1
Performance comparisons of FFTM and FFTM Clustering methods in terms of accuracy and CPU time

Distance between bubbles	Average error (%)	FFTM Clustering (s)	FFTM (s)
$2.5r$	0.35	1.54	1.26
$3.0r$	0.22	1.37	1.44
$4.0r$	0.05	1.16	1.67
$5.0r$	0.04	1.16	1.88
$6.0r$	0.05	1.16	2.89

5.1. Single bubble

Let us consider a single bubble immersed in an infinite fluid domain with an initial radius of $R'_0 = 0.1499$. For a specific heats ratio of $\lambda = 1.25$, this bubble will expand spherically to a maximum radius of 1.00 [12]. For this example, the simulations were carried out using FFTM and standard BEM for 2200 time steps, with a fixed time step size of $\Delta t' = 0.001$. The standard BEM took 11,572 s to complete the whole simulation, while FFTM needed only 2376 s, i.e. FFTM performed faster than the standard BEM by about 4.9 times.

A comparison of the bubble radius in its evolution is made between the numerical and theoretical results (as governed by the Rayleigh–Plesset equation). Fig. 3 shows the bubble radius as a function of time obtained from the FFTM and standard BEM together with the solution of the Rayleigh–Plesset equation (using a fourth-order Runge–Kutta method). As shown in Fig. 3, the FFTM curve agrees well with the analytic curve and it practically coincides with the results from the standard BEM. The maximum radius of the bubble calculated by FFTM and standard BEM are 1.006741 and 1.006739, respectively, which are less than 1.0% error as compared to the theoretical prediction. The numerical error in the maximum bubble radius between FFTM and standard BEM solver is 0.02%. This suggests that FFTM is a good approximation of the standard BEM solver.

Further comparison is made with respect to the relationship between the bubble surface velocity $\mathrm{d}R'/\mathrm{d}t'$ and radius R'. The analytical solution is given by [6]

$$\frac{3}{2}\left(\frac{\mathrm{d}R'}{\mathrm{d}t'}\right)^2 = -1 + R'^{-3}\left[1 + \frac{\varepsilon R_0'^{3\lambda}}{\lambda - 1}\left(1 - R'^{-3(\lambda-1)}\right)\right]. \tag{19}$$

Fig. 4 depicts the theoretical curve from Eq. (19) and the numerical results from the FFTM and standard BEM, which apparently shows good agreements. At the extreme of the negative part or minimum $\mathrm{d}R'/\mathrm{d}t'$, we observed relatively larger errors, which is likely due to the accumulations of numerical errors throughout the bubble simulation.

5.2. Two bubbles

Consider two oscillating bubbles with their centers initially placed on the x-axis at a dimensionless distance of 5.357 apart. Each bubble has an initial radius of $R'_0 = 0.1499$, and the simulations were carried out for 2200 time steps with time-step of $\Delta t' = 0.001$, as in the previous example.

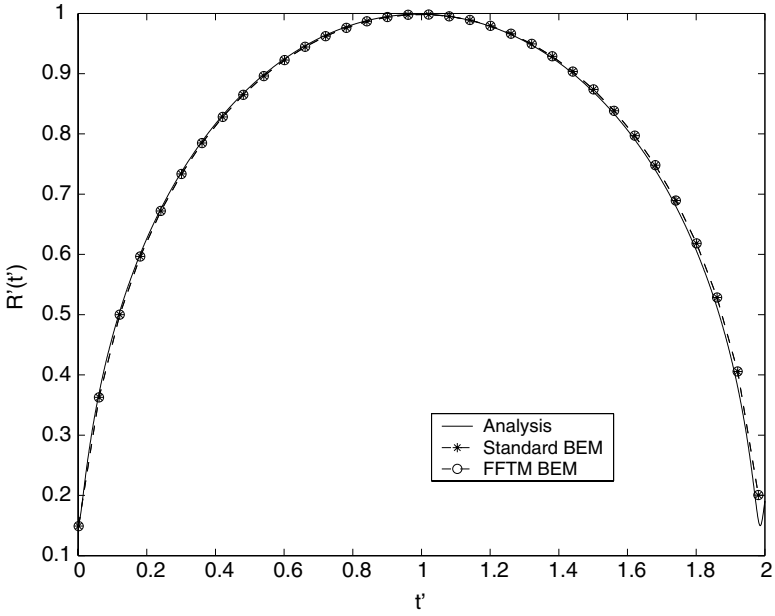

Fig. 3. Comparison of analytic Rayleigh bubble radius R' as a function of time t' with the FFTM and standard BEM. For the numerics, the bubble was generated with 642 nodes and 1280 triangular elements.

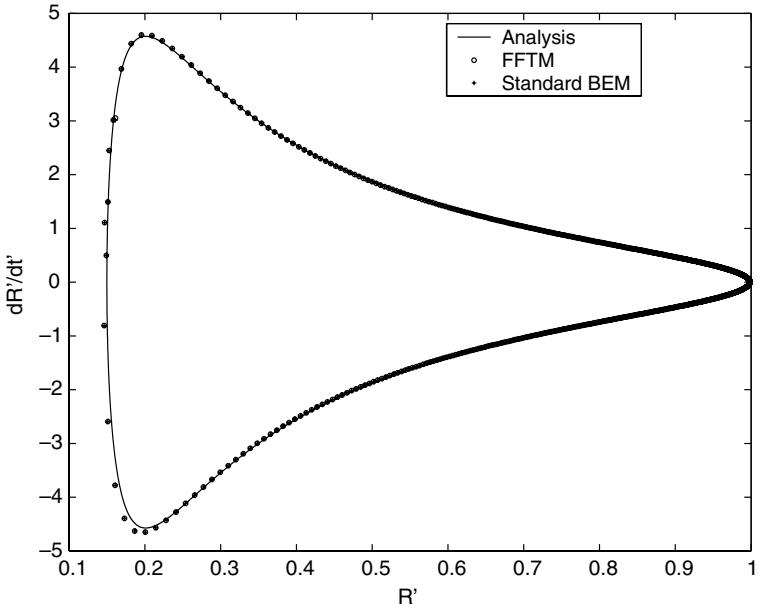

Fig. 4. Comparison of dR'/dt' vs. R' with FFTM and standard BEM. For the numerics, the bubble was generated with 642 nodes and 1280 triangular elements.

The results of the FFTM and FFTM Clustering methods are compared with that obtained by the standard BEM, where the average error is measured in the L_2 norm, similar to that defined in Eq. (18) except that it is now gauged against the standard BEM. The quantitative plots of the errors for the two methods are given in Fig. 5, which were less than 1.0% throughout the entire simulations. In terms of the bubbles evolution, the bubbles shapes from the three methods were essentially indistinguishable (not shown).

Fig. 6 shows the CPU times taken at the various stages for the entire simulations. At the initialization stage of each time-step, the FFTM approach took about twice the CPU time to compute the numerous

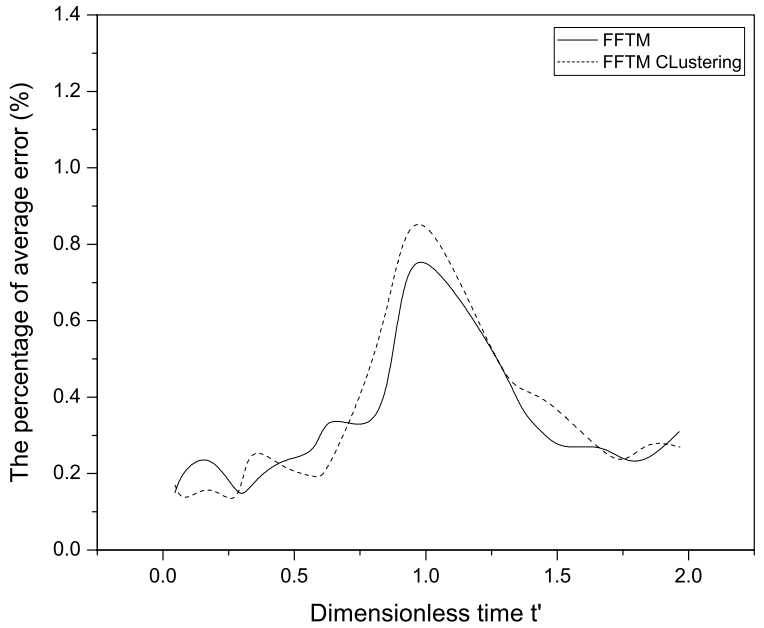

Fig. 5. Average error produced by the FFTM and FFTM Clustering of the normal velocities on two bubbles as compared with the standard BEM.

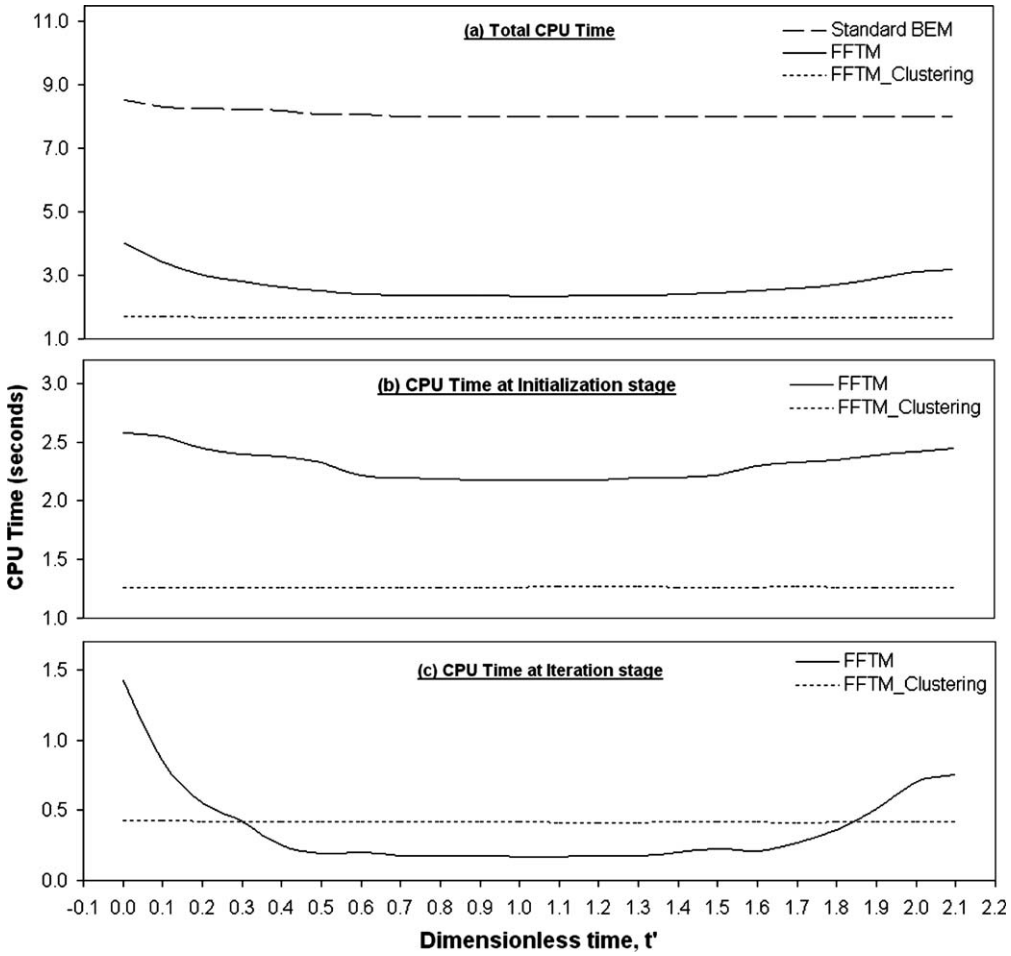

Fig. 6. CPU times taken for each time step for FFTM (solid-lines) and FFTM Clustering (dashed-lines), during the evolution of the two bubbles.

transformation matrices, as compared to the FFTM Clustering. It is also observed that the initialization times for the FFTM is slightly more when the bubbles were small, i.e., at the beginning of expansion phase and the later part of collapse phase. For the FFTM Clustering, the time taken remains relative constant throughout the simulations, as depicted in Fig. 6(b). On the CPU time for iteration stage (Fig. 6(c)), it is observed to vary quite drastically for the FFTM approach. This is again largely due to the changing sparseness of the problem as the bubbles evolved. In particular, the sparseness reduces as the bubbles expand, and hence attaining the fastest solve when they reach the maximum volumes at $t' = 1.077$. The bubbles then start to contract, which means that the void portion in the domain increases, which led to the decrease in efficiency of the FFTM method. While the efficiency of FFTM varies, that of the FFTM Clustering remains relatively constant throughout the whole simulation. A similar trend is observed for the total CPU time taken at every time step, as plotted in Fig. 6(a), which suggests that the FFTM Clustering is better able to deal with sparse problems more efficiently. Fig. 6(a) also depicts the CPU time taken by the standard BEM. It is found that the FFTM performed faster than the standard BEM by about 3 times, while the FFTM Clustering is faster than the latter by about 4.8 times.

5.3. Efficiency of the FFTM Clustering on multiple bubbles

In the previous sections, the FFTM Clustering has shown its superior performance on the test cases for one or two bubbles. It performs up to about five times faster than the standard BEM even for such small problems.

In this section, further tests with more bubbles are carried out to study its performance with increasing problem sizes. Here, we consider five examples with two, four, six, eight and twelve bubbles, respectively. The locations of bubbles for the various examples are as follows:

(1) Two bubbles: (0, 0, 0) and (0, 0, 5).
(2) Four bubbles: (0, 0, 0), (0, 0, 5), (0, 5, 5), (0, 5, 0) and (5, 0, 0).
(3) Six bubbles: (0, 0, 0), (0, 0, 5), (0, 5, 5), (0, 5, 0), (5, 0, 0) and (5, 0, 5).
(4) Eight bubbles: (0, 0, 0), (0, 0, 5), (0, 5, 5), (0, 5, 0), (5, 0, 0), (5, 0, 5), (5, 5, 5) and (5, 5, 0).
(5) Twelve bubbles: (0, 0, 0), (0, 0, 5), (0, 5, 5), (0, 5, 0), (5, 0, 0), (5, 0, 5), (5, 5, 5), (5, 5, 0), (10, 0, 0), (10, 0, 5), (10, 5, 5) and (10, 5, 0).

Each bubble is generated spherically with an initial dimensionless radius of $R'_0 = 0.1499$. Note that the CPU time taken by the standard BEM method for a large-scale problem (for example the eight bubbles and twelve bubbles) does not permit one to undertake 2200 time steps as in the previous sections. Therefore, we conducted only 50 time steps for these larger examples.

The results from the standard BEM and FFTM Clustering show indistinguishable bubbles shapes and features. According to the L_2 norm error denoted by Eq. (18), the average errors with the standard BEM as the reference at the end of 50 time steps range from 0.21% to 0.24% for the above-mentioned five configurations of multiple bubbles arrangement. Next, Fig. 7 shows the average CPU time taken in one time step for the FFTM Clustering and standard BEM. In the twelve bubbles example, the FFTM Clustering needed only 8.1 s, while the standard BEM used 457.1 s. The efficiencies of the FFTM and FFTM Clustering solvers are also studied with the speedup factor, defined as speedup $= \frac{T_{\text{std\_BEM}}}{T_{\text{FFTM\_solver}}}$, where $T_{\text{std\_BEM}}$ and $T_{\text{FFTM\_solver}}$ are the CPU time-staken by the standard BEM and the FFTM/FFTM Clustering solvers, respectively. The speed-up factors for the various examples were tabulated in Table 2, and it is observed to improve significantly when the number of bubbles (or problem size) increases.

In this section, we demonstrated that the FFTM Clustering method is an accurate and efficient fast algorithm as compared to the standard BEM. It was also shown to be more efficient than the original FFTM method for solving spatially sparse problems. In the following section, we employed the newly devised fast algorithm to study the physics of multiple bubbles dynamic problems.

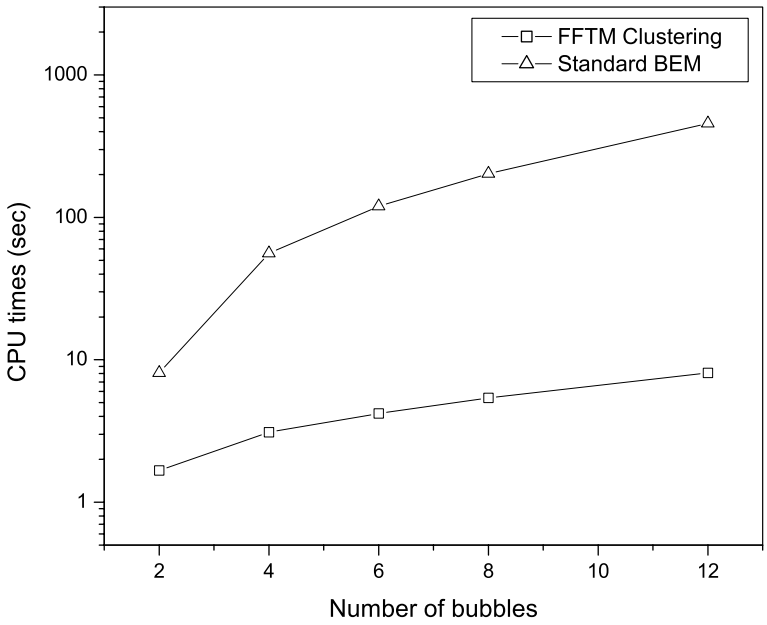

Fig. 7. Comparison of CPU time needed for one time step taken by the FFTM Clustering and the standard BEM.

Table 2
Speedup factor of FFTM Clustering method for multiple bubbles problems

Number of bubbles	Problem size (No. of nodes)	Speedup factor
2	1284	4.9
4	2568	18.2
6	3852	29.1
8	5136	37.5
12	7704	56.4

6. Some physics on multiple bubbles

Finding the direction of the bubble-induced jet in a single bubble in the midst of multiple bubbles has important implications for many engineering applications. Take for example, in ultrasonic cleaning of electronic components or medical equipments, multiple bubbles are created with accompanying bubble-induced jets directed towards the solid rigid surfaces for the removal of foreign bodies. An optimum or closed-to optimum timing of bubble initiation and distribution has yet to be worked out. Similarly in the bio-medical application of shock wave lithotripsy treatment (the removal of kidney stones), the pressure of induced jets due to collapsing bubbles near the solid wall is the main mechanism for the destruction of the kidney stones. Therefore, a study of multiple bubble behavior will enhance our understanding of the associated physical phenomena in these fields. We will now present several case examples to study the dynamics of multiple bubbles. All simulations shown here are fully three-dimensional and each bubble is generated with 362 nodes and 620 triangular elements on its surface. Only the FFTM Clustering method is employed.

Case 1. In the first example, we consider three bubbles initiated at the same time and their centers are initially placed on the x-axis. The location of these bubbles in dimensionless form are: (0, 0, 0), (2.68, 0, 0), (5.36, 0, 0). Each bubble starts to expand from a spherical shape with radius $R'_0 = 0.1499$.

Fig. 8(a) shows the shapes of the bubbles on the sliced plane of $z' = 0$ during the expansion phase, at the dimensionless times: $t' = 0.050$, $t' = 0.459$ and $t' = 0.829$. The center bubble is noted to be stretched slightly in the y' direction, and the two outer bubbles are seen to be pushed away a little from the center bubble. Fig. 8(b) shows the bubbles shapes at the dimensionless time $t' = 2.303$ in the collapse phase. It is clear that the center

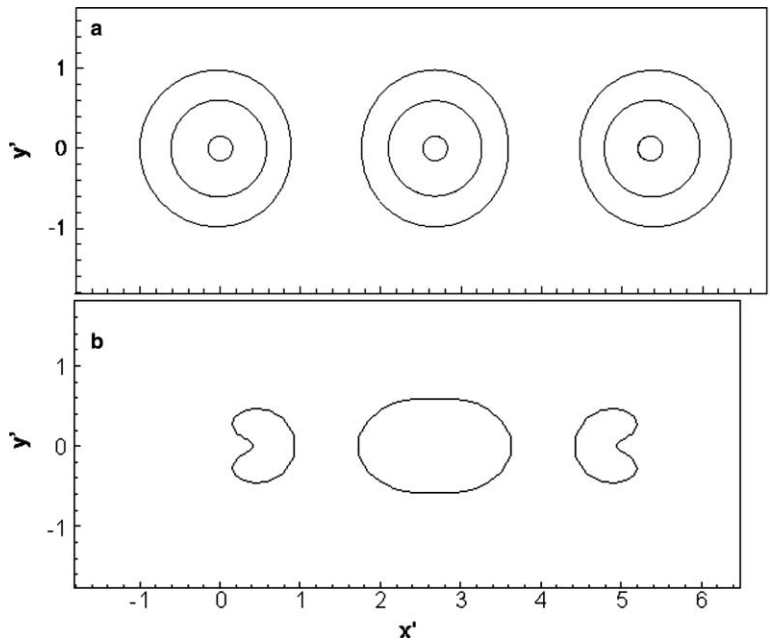

Fig. 8. Case 1. (a) The bubble shapes during the expansion phase at dimensionless time $t' = 0.050$, $t' = 0.459$ and $t' = 0.829$. (b) The bubble shapes during the collapse phase at dimensionless time $t' = 2.303$.

bubble is now stretched along the x'-axis, while the outer bubbles are attracted to the center of the system with induced-jets directed towards it.

Case 2. In this case, we consider three bubbles initiated at the same time but with different initial radii, namely; the center bubble has an initial bubble radius of $R'_0 = 0.1499$, while the outer two bubbles have $R'_0 = 0.2379$. The center bubble would have attained a maximum radius of 1.0 (if it were alone), while the two outer bubbles would have radii of 1.56. The bubbles are placed further away from each other due to their expected larger radii (in order to avoid coalescence [12]). Their center locations are given by (0, 0, 0), (3.55, 0, 0) and (7.10, 0, 0), respectively.

The three bubbles expand fairly spherically during the expansion phase as shown in Fig. 9(a). The center bubble is being slightly compressed by the two outer ones, which in turns are being pushed slightly outwards. Due to the differences in the initial radii, the center bubble is observed to start collapsing, while the outer ones are still in their expansion phases. This has led to a completely different evolution of the bubbles as compared to Case 1 in the collapsing phase. Fig. 9(b) shows the state at which the outer bubbles had attained their full expansion, while the center bubble in the collapsing phase has shown to develop some "necking" phenomenon at the mid-portion. Furthermore, the outer bubbles hardly move during the collapsing phase, unlike in Case 1, which is attributed to their larger masses associated with increased initial (and thus also maximum) volumes. Fig. 9(c) captures the three-dimensional view of the "necking" phenomenon in Case 2.

Case 3. In this example, we consider the arrangement of four bubbles initiated at the same time with initial radii $R'_0 = 0.1499$. The bubble centers are placed at the dimensionless locations: (2.68, 0, 0), (−2.68, 0, 0), (0, 2.68, 0) and (0, −2.68, 0). Note that this case is a baseline study for the subsequent two cases, where we will investigate the effects of the presence of an additional bubble placed at the center of the system.

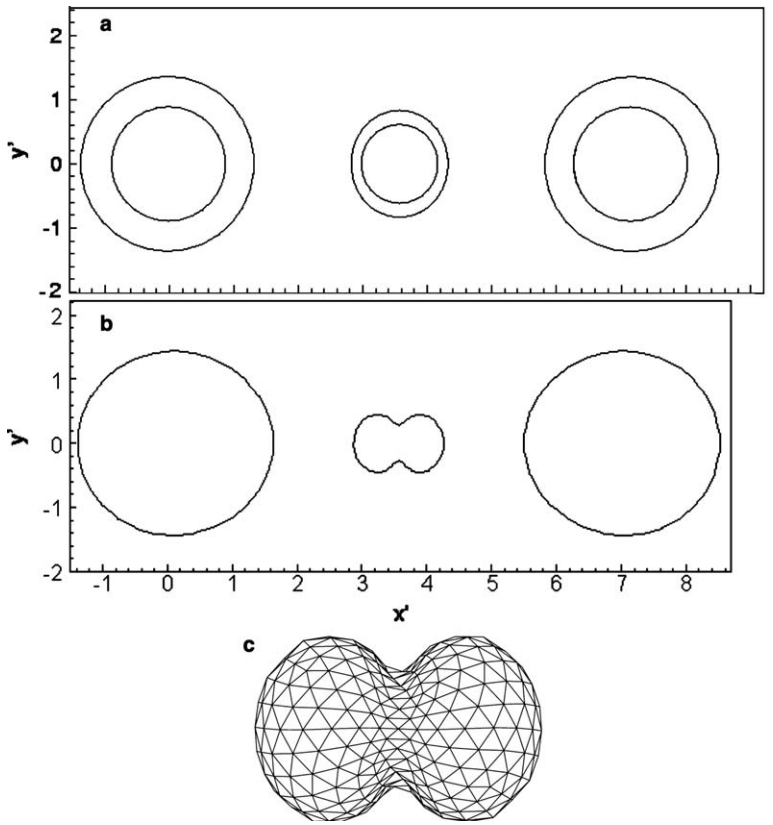

Fig. 9. Case 2. The shapes of three bubbles: (a) during the expansion phase at the dimensionless time $t' = 0.050$ and $t' = 0.758$, and (b) after full expansion at dimensionless time $t' = 2.65$. (c) Three-dimensional view of the center bubble in (b) with "necking" effect developed at mid-portion.

Fig. 10(a) shows the expansion phase where the bubbles expand quite symmetrically until they reach their maximum radii. Then, as the collapse phase begins and proceeds further, each of the bubbles exhibits an induced jet directed towards the geometrical center of the system as shown in Fig. 10(b). Fig. 10(c) captures

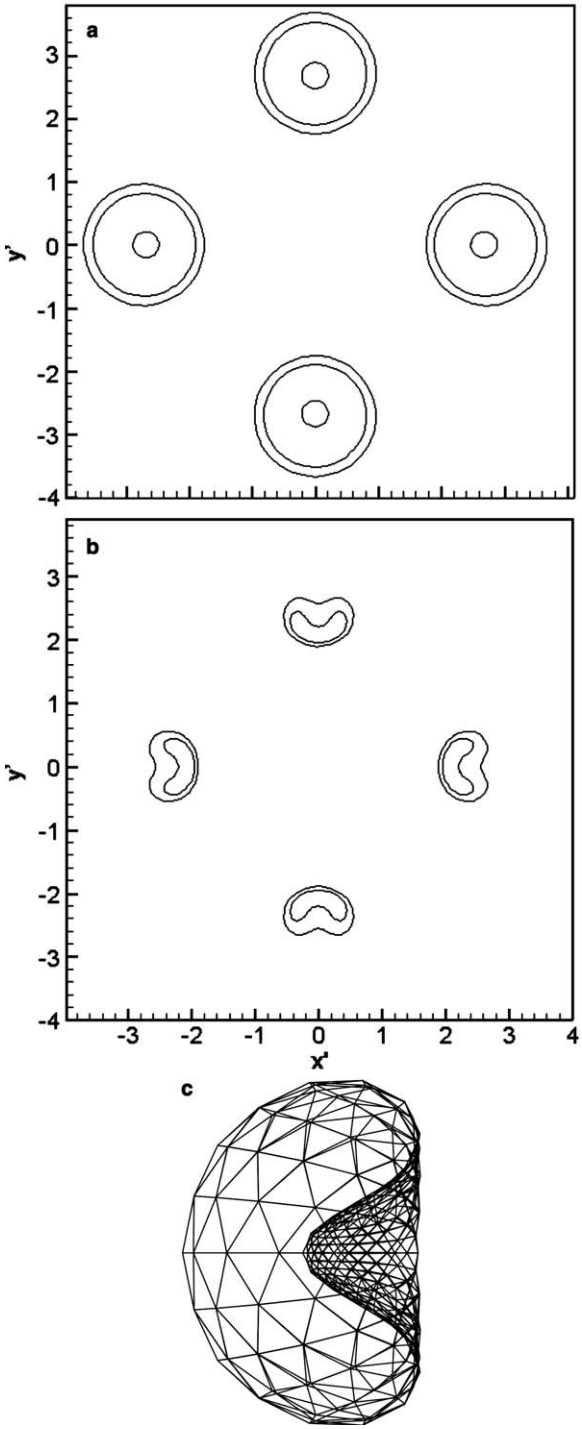

Fig. 10. Case 3. The shapes of four bubbles during the: (a) expansion phase at the dimensionless time $t' = 0.019$, $t' = 0.459$ and $t' = 0.830$, and (b) collapse phase at dimensionless time $t' = 2.418$ (bigger bubble size) and $t' = 2.479$ (smaller bubble size). (c) Three-dimensional views of the right outer bubble in (b) with an induced-jet.

the three-dimensional shape of the formation of the induced jet, which depicts the adequacy of the triangular elements in resolving the evolving jetting process.

Case 4. Here, the initial configuration of the four bubbles is the same as in Case 3, except that we now initiated at the same instance an identical fifth bubble at geometrical center, (0, 0, 0).

The five bubbles expand until they reach about their maximum radii as shown in Fig. 11(a). During the expansion phase, the outer bubbles deviate slightly from their spherical form and they move slightly outwards; the center bubble on the other hand, remains almost spherical. Then the outer bubbles begin their collapse phase with the bubble surface deforming and developing induced-jets directed towards the center of the system, as shown in Fig. 11(b). The outer bubbles are also noted to move towards the geometrical center of the system. In general, the dynamics of the four outer bubbles are similar that in Case 3. However, it is worthy to

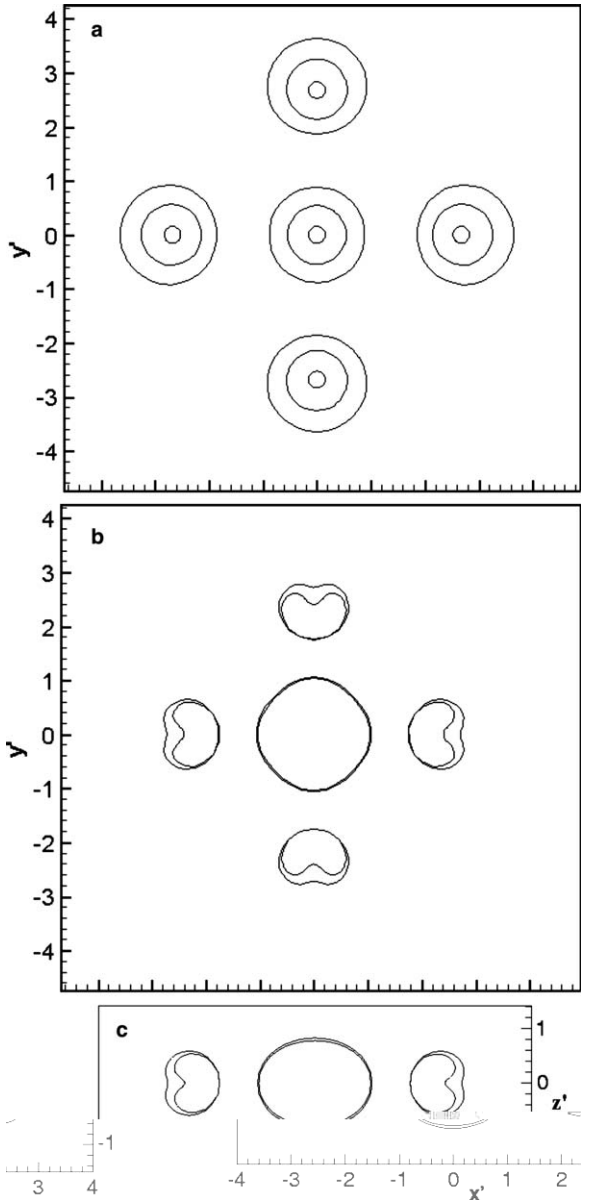

Fig. 11. Case 4. The shapes of five bubbles during: (a) the expansion phase at $t' = 0.005$, $t' = 0.175$ and $t' = 0.768$, and (b) the evolution after full expansion at the dimensionless time $t' = 2.145$ and $t' = 2.445$ ($z' = 0$ plane). And (c) shows the three bubbles viewed on the $y' = 0$ plane at the same time frame in (b).

observe that the presence of the center bubble (slightly) slows down the formation and evolution of the induced-jets (see the differences in the bubble profiles at approximately the same dimensionless time frame, i.e. Fig. 10(b) at $t' = 2.479$ and Fig. 11(b) at $t' = 2.445$). An even more interesting observation is that the center bubble is "prevented" from contracting during this collapse phase by the outer four bubbles. The center bubble takes on a "diamond" shape on the x'–y' plane but looks elliptic in the x'–z' plane (see Fig. 11(c)). The ambient pressure far away from the bubbles (dimensionless value 1.0) is much higher than the pressure inside the bubbles (due to over-expansion this value is much smaller than 1.0). This causes the outer bubbles to contract with development of the jet directed at the system center. On the other hand, the center bubble is largely "shielded" from this ambient pressure by the presence of the four outer bubbles and therefore it is expected to collapse at a much later time. Note that a similar simulation was performed by Chahine [33], which also shows the central bubble changes rather insignificantly relative to the four outer bubbles depicting the jet formation directed towards the geometrical center.

Case 5. In this case, we initiate the fifth bubble at a later dimensionless time of $t' = 1.0$, at which the four outer bubbles would be almost reaching their full expansion states.

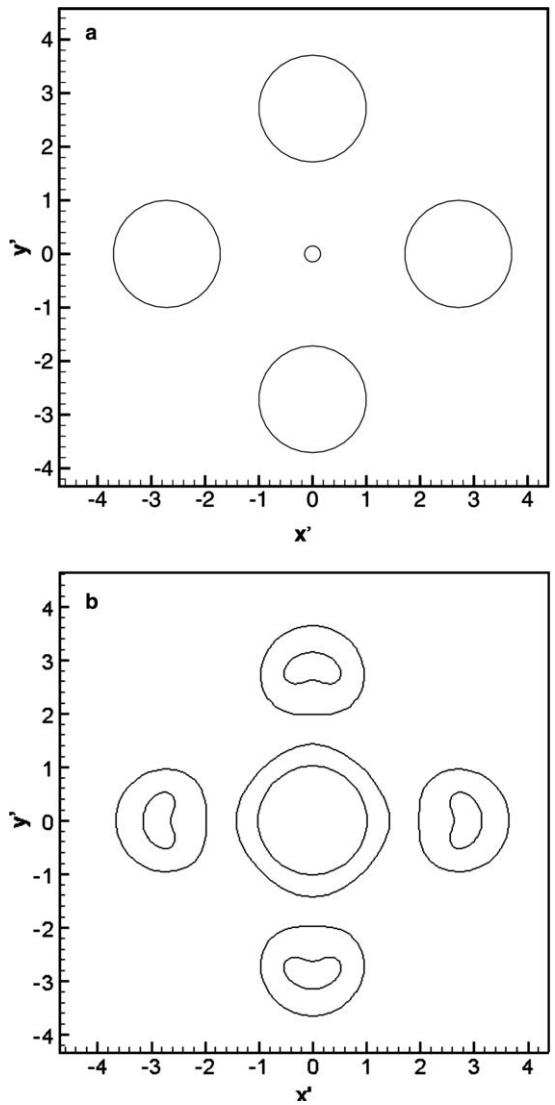

Fig. 12. Case 5. The bubble shapes at the dimensionless time: (a) $t' = 1.023$, where the outer bubbles have nearly reached their maximum volumes, while the center one is at its early stage of expansion. (b) At $t' = 1.499$ and $t' = 2.144$, where the outer bubbles are in the collapse phase, while the center one is at its expansion phase.

Fig. 12(a) shows the shapes of the five bubbles at the dimensionless time of $t' = 1.021$. The four outer bubbles have nearly reached their maximum, while the fifth center bubble is still at the beginning stage of the expansion phase. Fig. 12(b) shows the bubbles shapes at the dimensionless of $t' = 1.499$ and $t' = 2.145$. It is clear that the center bubble is still in the expansion state, although the bubble shape is much less spherical as compared to its earlier stage. This is attributed to the presence of the outer bubbles, which have very low internal pressure and exhibit a "suction" effect on the centre bubble surface. On the other hand, the outer bubbles are in their collapse phase and as these bubbles contract, liquid jets are directed outward of the system. This is exactly opposite from that in Case 4, where the induced jets were directed towards the geometrical center of the system. Hence from this study, we see that the timing of the creation of the innermost bubble would determine the direction of the jets induced on the outer bubbles.

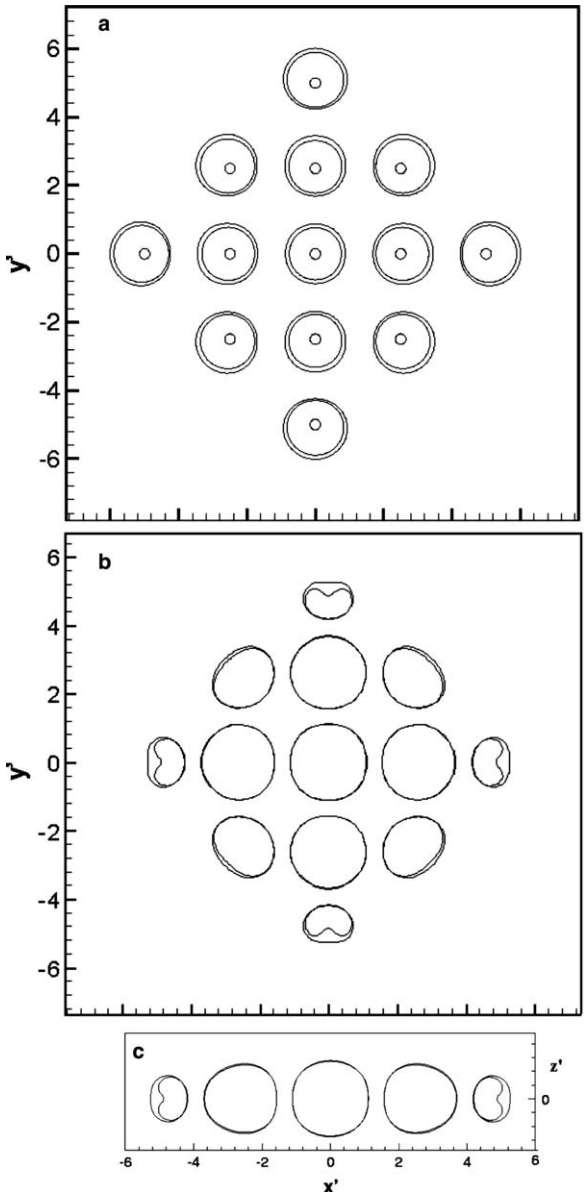

Fig. 13. Case 6. The shapes of bubbles during: (a) the expansion phase at the dimensionless time $t' = 0.050$, $t' = 0.605$ and $t' = 0.970$ (near the maximum volume), (b) the collapse phase at the dimensionless time $t' = 2.534$ and $t' = 2.646$ ($z' = 0$ plane). And (c) shows the five bubbles viewed on the $y' = 0$ plane at the same time frame in (b).

Case 6. For the next two examples, we aim to show the capability of the FFTM Clustering on modeling the bubbles dynamics of large-scale problem with numerical checks with previous works. First, we simulate the dynamics of thirteen bubbles initiated at the same time. Each bubble starts to expand from the initial bubble radius of $R'_0 = 0.1499$. This arrangement of the initial bubbles is similar to the example found in Blake et al. [3].

Fig. 13(a) shows the bubbles shapes during the expansion phase. All the bubbles except the center bubble expand with their centers moving slightly outwards. Then at the collapsing phase, the four outermost bubbles lying on the x' and y' axes deform most rapidly forming jets directed towards the center. The four bubbles lying on the diagonals deform at a much slower rate, but still exhibit the formation of jets at their beginning stage. At the meantime, the five innermost bubbles remain practically unchanged, as shown in Figs. 13(b) and (c). The relative higher pressure of the surrounding field has caused the outer boundaries of the said eight outer bubbles to move towards the geometrical center of the system, while the inner bubbles are largely shielded by these outer bubbles.

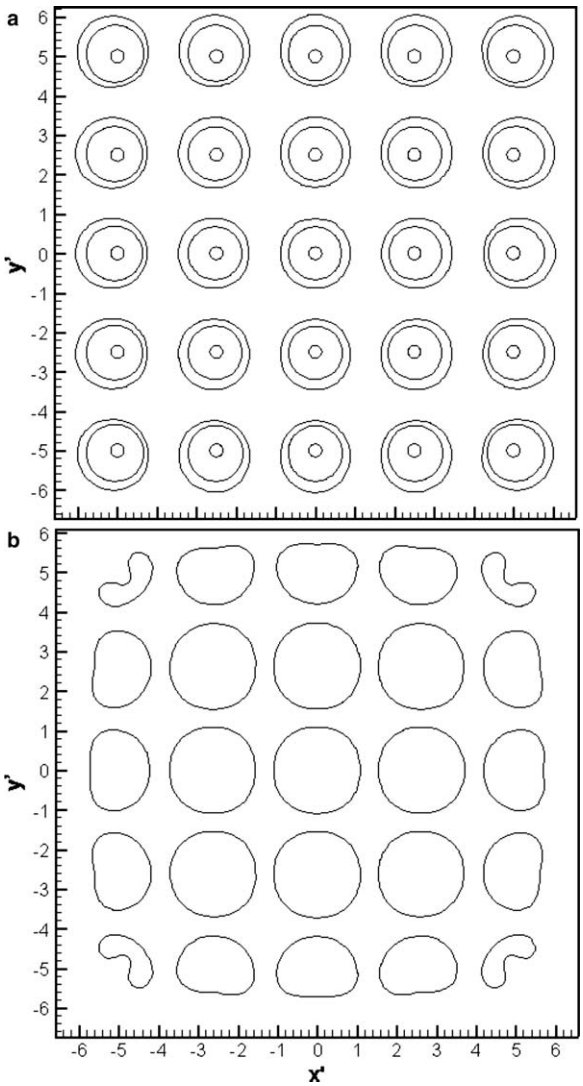

Fig. 14. Case 7. The shapes of bubbles: (a) during expansion phase at dimensionless time $t' = 0.010$ (most inner bubbles shapes), $t' = 0.473$ and $t' = 0.923$ (most outer bubble shapes), and (b) during the collapse phase at the dimensionless time $t' = 2.939$.

Note that the bubbles in the work of Blake et al. [3] were placed slightly closer to each other. Nevertheless, the observed physical behaviors bear some resemblance. Incidentally, Blake et al. [3] also seem to have used a multipole representation for the velocity potential and a lower order spherical harmonic for each bubble surface. However, not much further details were provided on the methodology and implementations, and other pertinent issues like quantitative tests on accuracy and efficiency.

Case 7. In this last case, we simulate for 25 bubbles exploding at the same time. Each bubble starts to expand from the initial bubble radius of $R'_0 = 0.1499$. The initial locations and shapes of the 25 bubble in the expansion phase are shown in Fig. 14(a). Similar to the previous case, the center bubble expand symmetrically, while all other bubbles expand with their centers moving slightly outwards from the center. As shown in Fig. 14(b) in the collapse phase, the outer bubbles deform with their respective jets directed towards the center of the system. At the meantime, the inner bubbles still keep to their respective relatively symmetrical shape. The four outermost bubbles located at the corners contract fastest and form the clearest jets directed inwards and towards the center of the system. The other remaining outer boundary bubbles on the four sides as indicated in Fig. 14(b) contract in volume followed by the formation jets as well (but slightly later than the corner bubbles). The inner bubbles take even longer before contracting in volume. At the dimensionless time of $t' = 2.939$, the inner bubbles still have their relatively spherical shapes. Fig. 15 zooms in on the bubbles shape in three-dimensions pertaining to the four bubbles located closest to the corner at $(-6.5, 6, 0)$. In Cases 6 and 7, a clear retardation effect of the innermost collapse can be observed. It is expected that this effect would be more significant if more bubbles oscillate in-phase at close distance from each other.

Chahine [33] performed a simulation with 21 identical bubbles in which all expanded at the same time and obtained very qualitatively similar gross features of the bubble dynamics as shown here; the outer bubbles collapsed earlier than the bubbles situated at the center of the system. The calculation by Chahine was performed using BEM code called 3DynaFS with only 102 nodes per bubble (as opposed to our 362 nodes for each bubble). It is unfortunate that no mention is made of the numerical method employed in 3DynaFS and the insufficiently detailed results have prevented a more quantitative comparison to be realized.

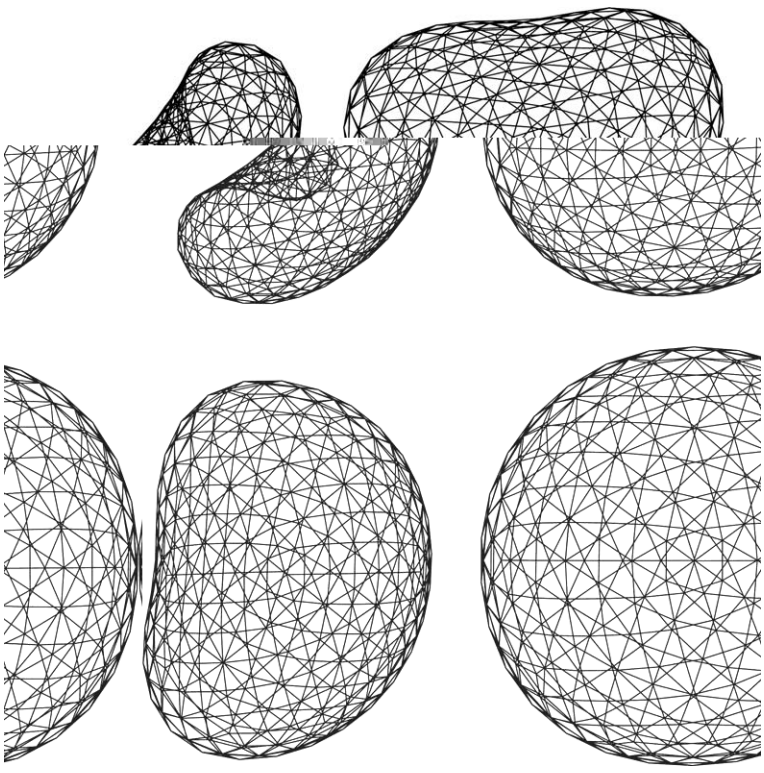

Fig. 15. Three-dimensional views of the four bubbles at the left-upper corner of Fig. 14(b).

7. Conclusions

In this work, we have implemented the FFTM algorithm to study the dynamics of multiple bubbles physics in the moving boundary problems. It is demonstrated that FFTM is an accurate and efficient method to simulate multiple bubbles in the moving boundary problems especially when the number of bubbles is large or the complex topology of the bubbles shapes is approximated with a large number of nodes and elements. However, a major drawback of the method is that its efficiency deteriorates quite significantly when the problem is full of empty spaces. A new version of FFTM Clustering is proposed. The FFTM Clustering is a generalized version of the FFTM algorithm. It is demonstrated that FFTM Clustering performs just as accurately as the FFTM, and the efficiency is less dependent on the distribution of bubbles in the problem domain.

The present work seeks to promote a fast BEM for industrial applications. It is shown that the use of advanced numerical algorithms can significantly improve the efficiency of multiple bubble simulations. This work also investigates some study cases of the multiple bubbles explosion. With the efficiency of the FFTM Clustering, it is feasible to study the complex physics of other multiple bubbles arrangements in future works.

References

[1] J.R. Blake, D.C. Gibson, Growth and collapse of a vapour cavity near a free surface, J. Fluid Mech. 111 (1981) 123–140.
[2] J.R. Blake, D.C. Gibson, Cavitation bubbles near boundaries, Annu. Rev. Fluid Mech. 19 (1987) 99–123.
[3] J.R. Blake, G.S. Keen, R.P. Tong, M. Wilson, Acoustics cavitations: the fluid dynamics of non-spherical bubbles, Phil. Trans. Roy. Soc. A 375 (1999) 251–267.
[4] S.A. Wilkerson, A boundary integral approach to three-dimensional underwater explosion bubble dynamics, Ph.D dissertation, Johns Hopkins University, 1992.
[5] R.H. Cole, Underwater Explosions, Princeton University Press, Princeton, NJ, 1948.
[6] C.E. Brennen, Cavitation and Bubble Dynamics, Oxford University Press, New York, 1995.
[7] L. Guerri, G. Lucca, A. Prosperetti, A numerical method for dynamics of non-spherical cavitation bubbles, in: Proceedings of the 2nd International Colloquium on Drops And Bubbles, 1981, pp. 175–181.
[8] Q.X. Wang, K.S. Yeo, B.C. Khoo, K.Y. Lam, Strong interaction between a buoyancy bubble and a free surface, Theor. Comput. Fluid Dyn. 8 (1996) 73–88.
[9] Q.X. Wang, K.S. Yeo, B.C. Khoo, K.Y. Lam, Nonlinear interaction between gas bubble and free surface, Comput. Fluids 25 (1996) 607–628.
[10] Y.L. Zhang, K.S. Yeo, B.C. Khoo, C. Wang, 3D jet impact and toroidal bubbles, J. Comput. Phys. 166 (2001) 336–360.
[11] Q.X. Wang, The evolution of a gas bubble near an inclined wall, Theoret. Comput. Fluid Dyn. 12 (1998) 29–51.
[12] S. Rungsiyaphornrat, E. Klaseboer, B.C. Khoo, K.S. Yeo, The merging of two gaseous bubbles with an application to underwater explosion, Comput. Fluids 32 (2003) 1049–1074.
[13] J.P. Best, A. Kucera, A numerical investigation of nonspherical rebounding bubbles, J. Fluid Mech. 245 (1992) 137–154.
[14] C.T. Kelley, Iterative Methods for Linear and Nonlinear Equations, SIAM Frontiers in Applied Mathematics, SIAM Philadelphia, 1995.
[15] Y. Saad, Iterative Methods for Sparse Linear Systems, PWS, Boston, 1996.
[16] A.W. Appel, An efficient program for many-body simulations, SIAM J. Sci. Statist. Comput. 6 (1985) 85–103.
[17] J. Barnes, P. Hut, A hierarchical O($N\log N$) force calculation algorithm, Nature 324 (1986) 446–449.
[18] L. Greengard, V. Rokhlin, A fast algorithm for particle simulations, J. Comput. Phys. 73 (1987) 325–348.
[19] L. Greengard, V. Rokhlin, A new version of the fast multipole method for the Laplace equation in three dimensions, Acta Numer. 6 (1997) 229–269.
[20] K. Nabors, F.T. Korsmeyer, F.T. Leighton, J. White, Preconditioned, adaptive, multipole-accelerated iterative methods for three-dimensional first-kind integral equations of potential theory, SIAM J. Sci. Statist. Comput. 15 (1994) 713–735.
[21] B.A. Luty, W.F. Gunstersun, Calculating electrostatics interactions using particle–particle–particle-mesh method with non-periodic long-range interactions, J. Chem. Phys. 100 (1996) 2581–2587.
[22] J.R. Phillips, J. White, A precorrected-FFT method for electrostatics analysis of complicated 3-D structures, IEEE Trans. Comput. Aided Design 16 (1997) 1059–1072.
[23] E.T. Ong, K.M. Lim, H.P. Lee, A parallel fast Fourier transform on multipoles (FFTM) algorithm for electrostatics analysis of three-dimensional structure, IEEE Trans. Comput. Aided Design 23 (2004) 1063–1072.
[24] E.T. Ong, K.M. Lim, K.H. Lee, H.P. Lee, A fast algorithm for three-dimensional potential fields calculation: fast Fourier transform on multipoles (FFTM), J. Comput. Phys. 192 (2003) 244–261.
[25] E.O. Brigham, The Fast Fourier Transform and its Applications, Prentice-Hall, Englewood Cliffs, NJ, 1988.
[26] S. Kapur, D.E. Long, IES3: Efficient electrostatic and electromagnetic simulation, IEEE Comput. Sci. Eng. 5 (1998) 60–67.
[27] P.L. Levin, M. Spasojevic, R. Schneider, Creation of sparse boundary element matrices for 2-D and axis-symmetric electrostatics problems using the bi-orthogonal Haar wavelet, IEEE Trans. Dielectric Elect. Insulat. 5 (1998) 469–484.

[28] A. Brandt, M. Spasojevic, R. Schneider, Multilevel matrix multiplication and fast solution of integral equations, J. Comput. Phys. 90 (1990) 348–370.
[29] M. Epton, B. Dembart, Multipole translation theory for the three-dimensional Laplace and Helmholtz equations, SIAM J. Sci. Comput. 16 (1995) 865–897.
[30] A.W. Appel, Handbook of Mathematical Functions, Dover Publications, New York, 1974.
[31] M. Frigo, S.G. Johnson, FFTW, C subroutines library for computing discrete Fourier transform (DFT) [Online]. Available from: <http://www.fftw.org>.
[32] T.T. Bui, A fast algorithm for modeling multiple bubbles dynamics, MEng Dissertation, National University of Singapore, 2005.
[33] G.L. Chahine, Strong interactions bubble/bubble and bubble/flow, in: J.R. Blake et al. (Eds.), Bubble Dynamics and Interface Phenomena, Kluwer Academic Publishers, Netherlands, 1994, pp. 195–206.